applied optics

# Phase imaging and detection in pseudo-heterodyne scattering scanning near-field optical microscopy measurements

Camilo Moreno,[1] Javier Alda,[1,2,*] Edward Kinzel,[3] and Glenn Boreman[1]

[1]Physics and Optical Science Department, University of North Carolina at Charlotte, 9201 University Blvd., Charlotte, North Carolina 28223, USA
[2]Applied Optics Complutense Group, University Complutense of Madrid, Av. Arcos de Jalón, 118. 28037 Madrid, Spain
[3]Mechanical and Aerospace Engineering, Missouri University of Science and Technology, 400W. 13th Str. Rolla, Missouri 65409-0050, USA
*Corresponding author: javier.alda@ucm.es

Received 19 October 2016; revised 20 December 2016; accepted 3 January 2017; posted 5 January 2017 (Doc. ID 279131); published 27 January 2017

**When considering the pseudo-heterodyne mode for detection of the modulus and phase of the near field from scattering scanning near-field optical microscopy (s-SNOM) measurements, processing only the modulus of the signal may produce an undesired constraint in the accessible values of the phase of the near field. A two-dimensional analysis of the signal provided by the data acquisition system makes it possible to obtain phase maps over the whole [0, 2$\pi$) range. This requires post-processing of the data to select the best coordinate system in which to represent the data along the direction of maximum variance. The analysis also provides a quantitative parameter describing how much of the total variance is included within the component selected for calculation of the modulus and phase of the near field. The dependence of the pseudo-heterodyne phase on the mean position of the reference mirror is analyzed, and the evolution of the global phase is extracted from the s-SNOM data. The results obtained from this technique compared well with the expected maps of the near-field phase obtained from simulations.** 

***OCIS codes:*** (120.5050) Phase measurement; (180.4243) Near-field microscopy; (240.6680) Surface plasmons; (350.4238) Nanophotonics and photonic crystals.

https://doi.org/10.1364/AO.56.001037

## 1. INTRODUCTION

Scattering scanning near-field optical microscopy (s-SNOM) allows measurement of evanescent fields with subwavelength resolution. This is possible because s-SNOM combines the high spatial resolution of atomic force microscopy (AFM) with additional illumination techniques to bypass the diffraction limit [1]. This has led to the popularity of s-SNOMs in recent years for imaging and obtaining optical information from structures such as nanoparticles [2], photonic-crystal waveguides [3], nanotubes [4], and even biomedical samples [5]. Our interest in s-SNOM is motivated by the study of near-field patterns produced by resonating metallic structures and optical antennas in the infrared [6,7]. However, the methods of signal analysis and interpretation of s-SNOM data require detailed attention [8,9]. In past years, modifications to the basic s-SNOM setup have been reported, such as the so-called phase-shifting interferometry technique [10] to retrieve near-field (NF) amplitude and phase, the homodyne technique [11] to measure attenuation and propagation constants for antennas, the pseudo-heterodyne technique [12] to enhance resolution and contrast in subsurface NF microscopy [13] or hybridization modes in antennas [14], and, more recently, the transmission-mode s-SNOM [15,16], which involves the illumination of antennas from below using linearly or circularly polarized light. Despite the fact that these techniques successfully retrieve amplitude and phase, the analysis is mainly based on the amplitude results, leaving room for a detailed analysis of the phase maps and for an improvement in the phase retrieval techniques ranging over the [0, 2$\pi$) interval. This contribution is focused on the use of data analysis techniques to assign the correct sign to the signal obtained for the sidebands of the harmonics used in pseudo-heterodyne techniques. Besides, the analysis presented in this paper allows a full understanding of the retrieved phase map when the global phase term appearing in the calculation is extracted from data.

In the s-SNOM technique, the sample is illuminated from the far field. The sample scatters this wave, producing both far- and near-field components. The near field contains information that is cut off by diffraction from propagation into the far field and would ordinarily remain undetectable. Figure 1

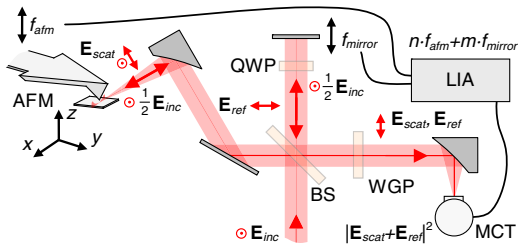


**Fig. 1.** Schematic of s-SNOM system with interferometer leg dithered for pseudo-heterodyne detection and a wire-grid polarizer for cross-polarized detection (BS, beam splitter; WGP, wire-grid polarizer; QWP, quarter-wave plate; LIA, lock-in amplifier; MCT, HgCdTe detector; AFM, atomic force microscope).

shows a diagram of the main elements and subsystems involved in the s-SNOM setup. The AFM tip locally interacts with the near field and scatters it into the far field. An optical system collects radiation scattered from the vicinity of the tip. This includes both radiation specularly reflected by the sample and other parts of the cantilever, as well as the tip-scattered near-field components. These specular components may be much larger than the near-field signal and constitute a background. It is necessary to suppress this background to extract the near-field information. This can be accomplished by dithering (vibrating) the AFM tip at a frequency $f_{\mathrm{AFM}}$. Because the amplitude of this vibration is small (typically 20 nm), the background specularly scattered signal does not vary significantly with respect to the dither frequency. However, the near field, which decays rapidly away from the surface, can be modulated by $f_{\mathrm{AFM}}$. The nonlinearity of the near-field contributions results in their better isolation from the background when detecting the second or third harmonic of this frequency.

The background signal is further suppressed by isolating the linear polarization orientation scattered by the tip. If we use a $XYZ$ coordinate system in Fig. 1, where the sample is placed on the $XY$ plane, the tip enhances the $E_z$ component. This becomes particularly effective if the $E_z$ component is cross-polarized with respect to the optical excitation. When the sample is illuminated by radiation polarized in the $X$ direction, much of the background signal can be blocked by a wire-grid polarizer transmitting only scattered radiation polarized along $Z$.

To obtain a map of the near field, the sample is moved in a raster-scan pattern under a static illuminating beam and a stationary cantilever tip driven in tapping mode. Besides the proper setting of the optical excitation and retrieval of the interferometric signal, an s-SNOM measurement requires an appropriate detection setup. The acquisition of the signal relies on the combination of an interferometer and a phase-locked detection to extract the frequency components of interest using a lock-in amplifier.

The use of the interferometer effectively amplifies the tip-modulated signal. It also allows the extraction of both the modulus and phase of the near field. To obtain the phase, the near-field signal is combined interferometrically with a reference signal, for which the absolute phase can be controlled. This reference signal is typically given by a reference leg that uses a flat mirror moved axially along its normal. One approach is to combine scans with successive registration of the interference signal for several axial positions of the reference mirror. These scans are used to fit the phase map [10,17]. Several detection techniques can be applied to better analyze the signals retrieved from the s-SNOM system. Among them, pseudo-heterodyne s-SNOM detection is effective for suppressing the background signal while providing a measurement of the modulus and phase of the electric-field component [12]. The pseudo-heterodyne approach modulates the reference phase and further suppresses portions of the signal that are not interacting with the interferometer. A main advantage of the pseudo-heterodyne technique is the capability to extract meaningful information from a single raster scan of the sample. This shorter acquisition time becomes an important advantage when considering optomechanical stability and the temporal drift of the measurement conditions. The usual alternative of homodyne detection needs successive scans, requiring a typical measurement duration of several tens of minutes and consecutive exposures of the cantilever tip to the sample. Temporal fluctuations over this timescale of the laser power [18] and the position of the focusing and collimation optics may produce signal deterioration over the data acquisition time. While these experimental limitations can be minimized to preserve a good signal, they cannot be eliminated. In this sense, pseudo-heterodyne techniques are superior for fragile samples and reduce the requirements for long-term stability in the experimental conditions.

From the measurement setup perspective, pseudo-heterodyne is based on the generation of sidebands around the harmonics of the cantilever movement. Practically, in a typical s-SNOM setup, these sidebands are produced by moving the mirror of the reference leg of the interferometer at a frequency $f_{\mathrm{mirror}}$ that obeys $f_{\mathrm{mirror}} \ll f_{\mathrm{AFM}}$. This is accomplished when the mirror is driven with a harmonic modulation, $s = s0 + A\cos(2\pi \cdot f_{\mathrm{mirror}})$. The modulation depth for the interferometer is then $\gamma = \pi A/\lambda_0$, where $A$ is the peak-to-peak displacement of the mirror, and $\lambda_0$ is the laser wavelength. Therefore, as outlined in [12], the electric field modulated by the reference mirror can be expanded as

$$E_R = \sum_m \rho_m \exp(im f_{\mathrm{mirror}} t), \tag{1}$$

where the coefficients $\rho_m = \rho J_m(\gamma)\exp(i\Psi_G + im\pi/2)$, and $J_m$ is the Bessel function of the first kind, $m$-th order; $\Psi_G$ accounts of the phase difference between the signal and the reference beam; $\gamma$ is the amplitude modulation. By the introduction of this modulation, the $n$th scattered signal harmonic with frequency $n \cdot f_{\mathrm{AFM}}$ splits into sidebands with frequencies $f_{n,m} = n \cdot f_{\mathrm{AFM}} + m \cdot f_{\mathrm{mirror}}$.

Background scattering can be removed by selecting the first and second sidebands ($m = 1, 2$). This means demodulating the detector signal at frequencies $n \cdot f_{\mathrm{AFM}} + f_{\mathrm{mirror}}$ and $n \cdot f_{\mathrm{AFM}} + 2f_{\mathrm{mirror}}$. These demodulated signals can be designated as $S_{n,1}$ and $S_{n,2}$. The pseudo-heterodyne measurement mode provides the modulus and phase of the electric near field backscattered from the sample from a proper combination of these sidebands. The previous expansion gives the ratio of the modulus of the sideband signals to be $|S_{n,1}|/|S_{n,2}| = J_1(\gamma)/J_2(\gamma)$. Setting a modulation depth of $\gamma = 2.63$ [12] makes the modulus of coefficients of the first and second

sidebands ($m = 1, 2$) equal. In our case, the second harmonic of the cantilever frequency ($n = 2$) produces good signal resolution and overall intensity. In this case, the complex amplitude of the near-field $E_z$ component is given as

$$E_z(x, y) = \kappa[S_{2,2}(x, y) - iS_{2,1}(x, y)] \exp[i\Psi_G], \quad (2)$$

where $\kappa$ is a real number that accounts for the detector response, the transmissivity of the SNOM optical system, and the reference beam amplitude, $\Psi_G$ is the global phase factor, and $S_{n,m}(x, y)$ are maps obtained by a raster scan of the sample under analysis. If the system is operated with a modulation depth different from $\gamma = 2.63$, these sidebands combine differently, and a proportionality factor $J_1(\gamma)/J_2(\gamma)$ appears, multiplying the contribution of the second sideband, where $\gamma$ is the actual modulation depth occurring in the system.

From Eq. (2), the modulus and phase of the near-field component, $E_z(x, y) = |E_z(x, y)| \exp[i\phi(x, y)]$, can be given as

$$|E_z(x, y)| = \kappa\sqrt{S_{2,2}^2(x, y) + S_{2,1}^2(x, y)}, \quad (3)$$

$$\phi(x, y) = \Psi_G - \Phi(x, y), \quad (4)$$

where

$$\Phi(x, y) = \tan^{-1}\left[\frac{S_{2,1}(x, y)}{S_{2,2}(x, y)}\right], \quad (5)$$

so that the selection of the modulation depth $\gamma = 2.63$ equally weights the real and imaginary portions represented by the signals. In practice, phase map variations do not depend on a constant phase level, and, typically, the global phase $\Psi_G$ is not considered. However, in Section 4 we will discuss how to reach and obtain this value from pseudo-heterodyne SNOM measurements as well. Signals $S_{2,1}$ and $S_{2,2}$ are obtained from a lock-in amplifier properly set to extract those values. Some previous analyses have been focused on the enhancement of the contrast of the signal for various cases of interest [19] and also have simulated how to combine different outputs from the lock-in amplifier [9]. If the lock-in amplifier is set to register the modulus of these signals, they are always positive valued. Maintaining this experimental setting produces an ambiguity in the phase value that is extracted from the measurement. From Eq. (5), and assuming positive values for the signals $S_{2,1}$ and $S_{2,2}$, $\Phi$ can only belong to the first and third quadrant. Some s-SNOM applications, where the expected phase variation is well restricted within one quadrant [12], can still provide significant and valuable near-field results using positive-valued signals. However, metallic resonant structures and optical antennas, where phase varies over $[0, 2\pi)$, need access to the whole angular range [6–8]. A restricted phase availability could be seen as the price to be paid for a simple data recovery method. However, showing some additional ambiguity, the value of $\Phi$ obtained from an equation that only allows positive arguments could be any one of four possible angles: $\Phi$, $\pi - \Phi$, $\pi + \Phi$, and $2\pi - \Phi$. These four angular values appear when considering the two possible choices of signs, ±, of both $S_{2,1}$ and $S_{2,2}$. How to resolve this ambiguity and maintain the simplest possible measurement strategy is one of the goals of this contribution. This ambiguity problem has been also encountered and solved for the homodyne detection mode in s-SNOM [20].

Section 2 presents a reliable method to properly combine $X$ and $Y$ components from the lock-in amplifier, providing quantitative parameters to understand better the goodness of the approach. Section 3 shows how this approach can be experimentally used with pseudo-heterodyne data obtained from an infrared s-SNOM system. In Section 4, to complete the analysis of the terms appearing in the phase evaluation [Eq. (4)], we have studied the role of the overall phase factor, $\Psi_G$, that arises from the mean position of the vibrating reference mirror, obtaining its value from a collection of pseudo-heterodyne measurements. Finally, Section 5 summarizes the main findings of this paper.

## 2. SIGNED MODULUS

The signal obtained from a lock-in amplifier actually has more information than a single modulus value. The lock-in detection scheme using two phase-locked amplifiers in quadrature, employed in most of the current lock-in amplifiers, produces a signal having a modulus, $R$, and an angle, $\alpha$, when represented in polar coordinates. Alternatively, it can be decomposed in rectangular coordinates as $X$ and $Y$ components, corresponding to the two phase-locked oscillators in quadrature. This capability makes it possible to extract not only the modulus of the signal, but also the "sign," or orientation, of this modulus. After checking the angle of the signal at a given point on the sample, the information from the modulus can be completed with the appropriate sign. Then, the calculation of the $\tan^{-1}$ can consider the signs of both signals, $S_{2,1}$ and $S_{2,2}$, and produces an angular value that could be at any point within the $[0, 2\pi)$ range. The whole range is accessed by using the two-argument version of the $\tan^{-1}$ function, which is typically denoted as atan $2(y, x)$. Although this signal treatment could require the retrieval of both the modulus and phase (or the $X$ and $Y$ components), it is possible to set the signal recovery system to recover the phase within the $2\pi$ range from one raster scan for each sideband. This can be done by zeroing the phase before proceeding with the measurement.

### A. Signal in Cartesian Coordinates

Obtaining a signal from a lock-in amplifier allows the establishment of the origin for the angle of the signal, $\alpha$. It is important to recall that the angle of the lock-in signal is referenced to the phase of both oscillators in quadrature. If we ideally assume that this angle is stable during the measurement time, it could be possible to lock one of the phase-locked oscillators (typically the one corresponding to the $X$ component) to the actual phase of the signal and register this component as the "signed" modulus of the signal. If the phase of the signal does not change too much, this component is quite close to the modulus value, i.e., $|X| \backsimeq R$. In this situation, the modulus remains positive, and the phase jumps between two possible values: 0 and $\pi$ (or $-\pi$). This setting in the lock-in amplifier is sometimes designated as zeroing the angle. This zeroing requires a signal stable and strong enough to avoid large fluctuations of the signal angle during the measurement process. However, sometimes the signal fluctuations and signal noise make the previous zeroing of the angle not fully trustworthy. In that case, it is safer to retrieve both $X$ and $Y$ components and post-process them to

have a more robust assignment of the sign. As we will see in Section 3, a proper rotation of the data within the $XY$ plane will align the data along a new axis, where the sign is better assigned. When registering both components, the s-SNOM measurements should provide four maps from the raster scan of the sample: the $X$ and $Y$ components for the two selected sidebands used in the pseudo-heterodyne mode.

From the previous analysis, we now think of the signals obtained from each sideband as $X$ and $Y$ components in a Cartesian coordinate system. Each location in the sample corresponds to a point in the $XY$ plane for each sideband, representing the corresponding sideband signal at that spatial location. Those points are distributed in the $XY$ plane, depending on the lock-in amplifier angular settings (or signal phase settings). If the angle of the signal was stable and constant along the whole measurement, and only changes in the modulus were observed when changing location on the sample, the measured points will align along a straight line. This line will also be oriented with an angle, $\alpha$, related to the phase shift between the measured signal and the local oscillators of the lock-in amplifier. In this ideal case, when zeroing the angle, points in the $XY$ plane will align along the $X$ axis, having a null $Y$ component. Actually, signals present angle fluctuations and drifts and are affected by noise. Therefore, the points on those planes describing the first and second sidebands are distributed as a scatter plot over the $XY$ planes. These scatter-plot distributions can be characterized by their mean and standard deviation. This characterization can be easily done by analyzing the covariance of the $X$ and $Y$ coordinates. When calculating the covariance matrix, we can apply diagonalization techniques, similar to the principal component analysis restricted to a two-dimensional case [21]. This diagonalization produces the values of the maximum and minimum variances, $\sigma_{\max}$, $\sigma_{\min}$, and the orientation of them, $\beta$. Since the maximum and minimum variances are oriented perpendicularly to each other, we only need the angular orientation, $\beta$, of one of them, typically the one corresponding to the maximum value, $\sigma_{\max}$. This procedure is similar to fitting an ellipse oriented along the directions where the scatter-plot is extended longer and shorter. In the following section, we will see how to apply this method to a practical case involving pseudo-heterodyne measurements from an infrared s-SNOM system.

## 3. EXPERIMENTAL RESULTS

An array of aluminum square patches, 2.2 μm in size on a 3 μm pitch, on a dielectric stand-off layer (bisbezonzcyclobutene, BCB) are measured using an s-SNOM system, as presented in Fig. 1. We select this sample because of its symmetry and simple near-field pattern. The s-SNOM is illuminated with a $CO_2$ laser source (Access Laser, model L4SL) operating at $\lambda = 10.6$ μm. The signal is detected using a HgCdTe liquid-nitrogen refrigerated detector from Judson Teledyne, (model J15D12-M204-S025U-60.) A Veeco/Bruker Innova atomic force microscope system (model AFM 1A325) with Pt-coated cantilevers (Arrow-NC, NanoWorld) at an approximate vibrating frequency of $f_{\mathrm{AFM}} = 280$ kHz is used. The signal is retrieved using a Zurich Instruments lock-in amplifier (model HF2LI) that drives a Physics Instruments piezostage (model E-665) attached to a Si mirror on the reference leg of the detection arm. The measurements are acquired using Veeco software for AFM applications and Zurich Instruments software. The status of the system (signal level at the detector and vibration range of the mirror) is monitored using an oscilloscope and a digital multimeter. The acquired data, containing topography and the $S_{2,1}$ and $S_{2,2}$ maps, were pre-processed for format compatibility and scaling using the WSxM [22] and Gwyddion [23] software and post-processed using MATLAB [24]. To compare different statuses of the measurement system, two sets of data are retrieved for slightly different configurations of the measurement station. This difference in the cantilever and the detector focusing settings makes data set A of better quality than B. In addition, the cantilever itself was changed between the two data set rounds. However, both data sets allow good modulus and phase characterization of the structures under analysis.

Figure 2 shows the maps obtained for a near-field s-SNOM measurement of data set A when splitting the signal into $X$ and $Y$ components, for the two sidebands used in our experiment. The actual configuration of the s-SNOM system used in this analysis does not allow simultaneous retrieval of those four signals ($X$ and $Y$ components of both sidebands). To obtain them, we make two consecutive scans of the sample. The first one retrieves the $X$ component, and the second one retrieves the $Y$ component. For data set A, we set $\alpha$ to zero in the lock-in amplifier, making the $X$ component larger than $Y$. The angle, $\alpha$, was intentionally not zeroed for data set B.

Signals in Fig. 2 for data set A can be represented as a data cloud. These data clouds are plotted in Fig. 3. We have represented with different colors the signals corresponding to the resonant patches (red) and to the substrate (blue). This segmentation of the data has been possible by using topographical information to distinguish between substrate and metal structures. Plots in Figs. 3(a) and 3(b) represent the original signal retrieved from the lock-in. It can be seen that the zeroing process has aligned these signals quite well along the X direction.

At this point, we pay attention to the center of the data cloud. For the sample analyzed in this paper, the near field is associated with the resonances of the metallic structures. Then, we may assume that the substrate should not contribute

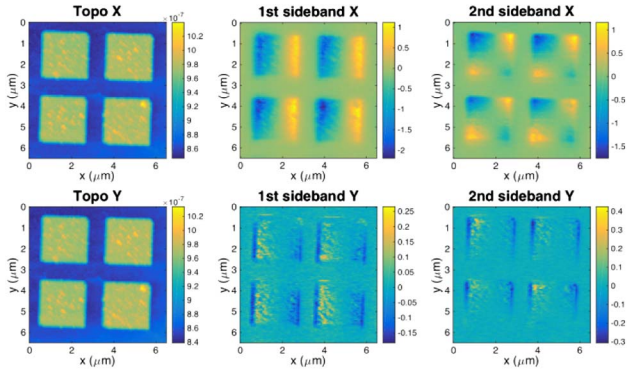


**Fig. 2.** Maps of the topography and $X$ and $Y$ components of the near-field signal extracted from the first and second sidebands in pseudo-heterodyne detection mode for data set A. The angle of the signal, $\alpha$, was set to zero before the measurement.

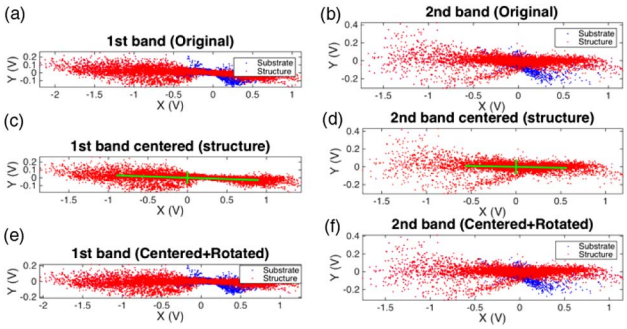


**Fig. 3.** Data cloud of the signals registered for the (a, c, e) first and (b, d, f) second sidebands. The original data are shown in plots (a) and (b). The signals from the structure are plotted in (c) and (d). In these plots, the signals are self-centered, and the straight lines in (c) and (d) represent the directions of the maximum and minimum variance of the data. The maximum-variance direction is slightly misaligned with respect to the $X$ axis. Figures (e) and (f) represent the original signal rotated to align data along the maximum-variance direction and centered to the mean of the data obtained from the substrate.

to the near-field signal. However, due to noise, the signal from the substrate is never exactly zero. In order to refer the measured signal to a given point, we have chosen this reference point as the mean value along the $X$ and $Y$ directions, taking into account only the substrate data. Therefore, signals are centered with respect to this reference point. For samples where the substrate contribution is significant, this reasoning should be adapted accordingly, looking for those regions in the sample where the near-field contribution should be zero. If those regions are not available, the centering of the data can always be made with respect to the mean value along $X$ and $Y$, considering all the points in the sample.

Additionally, when analyzing the variance of the data set, we may see that the maximum variance and minimum variance directions, represented in plots (c) and (d) of Fig. 3, are not exactly oriented along the $X$ and $Y$ directions, as desired. The orthogonal segments represented in Figs. 3(c) and 3(d) have a length proportional to the root mean square variation, $\sigma$, along the directions of the minimum and maximum variance. Then, a rotation of the data cloud should provide a better result because this rotation aligns the signals that will be used in Eqs. (2) and (4) along the direction of the largest variation. The rotation angle, $\beta$, is obtained from the variance evaluation. This rotation is presented in plots in Figs. 3(e) and 3(f), where the data also have been centered using the mean of the signal from the substrate. The value of $\beta$ is also presented in Table 1.

From the previous results, it is possible to apply Eqs. (2) and (4) to obtain the modulus and phase of the near field generated by the resonant structures under test using the data along the direction of the maximum value of the variance. In Fig. 4, we show the near-field results obtained from the first and second band measurements presented in Figs. 2 and 3. Figures 4(a) and 4(b) show the results when no sign is retrieved from the experiment. However, when taking into account the method described in this paper, it is possible to determine the sign for the first and second band signals. Then, Figs. 4(c) and 4(d) show the near-field maps obtained when using the $X$ component. As an example of what could happen if the orientation of the data cloud is not properly done, we represent in Figs. 4(e) and 4(f) the near field obtained using the $Y$ component. The results in Figs. 4(c) and 4(d) agree very well with the expected modulus and phase obtained from HFSS simulations [25] for the resonant structure under analysis [plots in Figs. 4(g) and 4(h)]. Although the modulus maps are quite similar for Figs. 4(a) and 4(c), there is quite a significant difference between the phase maps in Figs. 4(b) and 4(d). When the sign of the signal is not considered, the phase map [Fig. 5(b)] is not reproducing the results expected from simulation. The agreement with the simulation results is clearly better when considering the $X$ component. At the same time, we can confirm how the application of Eq. (3) to the unsigned modulus is constrained within the $[0\ \pi/2)$ range [see Fig. 5(b)].

**Table 1. Rotation Angle, $\beta$, and Relative Weight, $w_{\max}$, along the Maximum Variance Direction for the Two Sidebands (Subscripts 1 and 2)**

| Data Set | $\beta_1$ (deg) | $w_{\max,1}$ | $\beta_2$ (deg) | $w_{\max,2}$ |
|---|---|---|---|---|
| A (structure) | −1.88 | 0.9950 | −1.08 | 0.9837 |
| A (substrate) | −2.29 | 0.9935 | −2.00 | 0.9777 |
| A (all) | −1.96 | 0.9945 | −1.45 | 0.9812 |
| B (structure) | −76.28 | 0.9517 | −71.75 | 0.9517 |
| B (substrate) | −66.39 | 0.8655 | −66.04 | 0.7884 |
| B (all) | −75.18 | 0.9370 | −71.65 | 0.9407 |

As we mentioned before, sometimes the zeroing of the absolute angle provided by the lock-in amplifier is not available, or it is not possible to sufficiently reduce fluctuations due to noise or other experimental contributions. In that case, the method proposed here can be still applied when considering both the $X$ and $Y$ components of the signal. This is the case of data set B, where noise is more significant than in data set A, and no zeroing procedure has been applied. Figure 5 shows how the original data are oriented along an oblique direction. This orientation is corrected by rotation and, after centering using the substrate data and rotating to align the data along the $X$ direction, it is still possible to process the data using the pseudo-heterodyne approach. Figure 6 shows the results obtained for this data set. When comparing these results to those presented in Fig. 4, we can see that the modulus is quite similar, and, at the bottom portion of the square patches, the phase is departing from the results obtained from data set A. This difference in the phase map can be explained when considering the effect of the global phase $\Psi_G$, which affects the location of the $2\pi$ phase wrapping boundary over the sample. Also, we show in this plot how the phase map would appear if only the unsigned modulus of both sidebands were used.

One of the advantages of this data process is that we can quantify the goodness of the proposed analysis. A quantitative parameter of this quality is the amount of variance explained along the direction of the maximum variance for the data set. This is given as

$$w_{\max} = \frac{\sigma_{\max}^2}{\sigma_{\max}^2 + \sigma_{\min}^2}, \tag{6}$$

where the denominator is the total variance of the data set. This parameter can be seen as a parameter that quantifies the quality

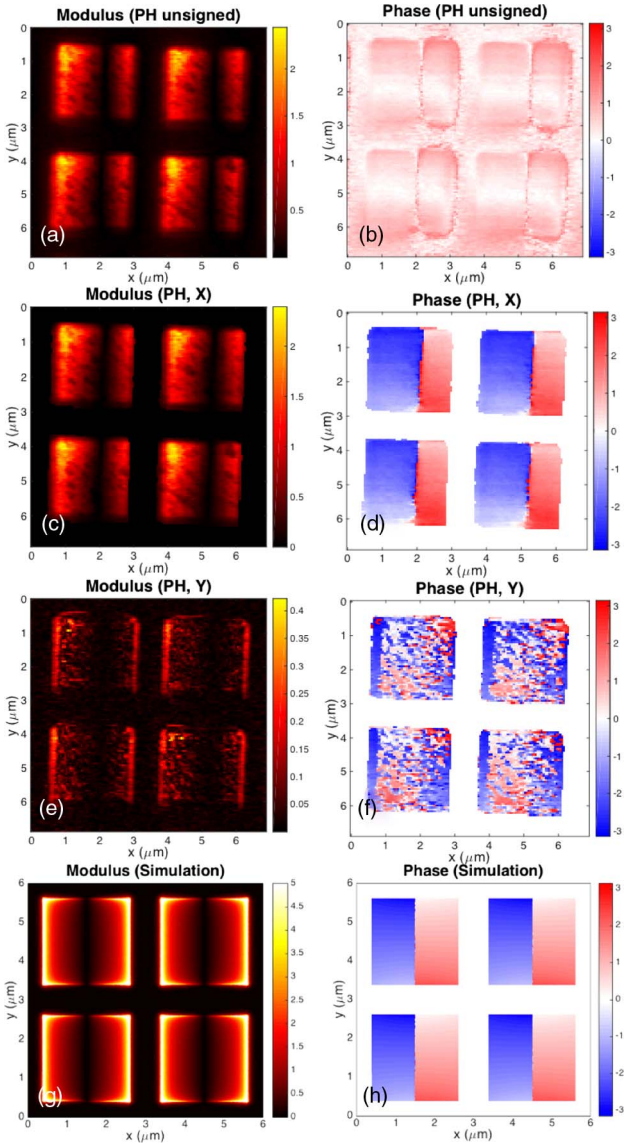


**Fig. 4.** (a, c, e, g) Near-field modulus and (b, d, f, h) phase, corresponding to the square patches structures for data set A. Plots (a) and (b) correspond to the results of Eqs. (2) and (3) for the unsigned modulus of the signal. The results obtained from the method proposed in this paper are shown in plots (c) and (d), where the field is obtained from the $X$ component of the signals. Plots (e) and (f) are obtained from component $Y$. Finally, these experimental results are compared with the simulations obtained from HFSS [see plots (g) and (h)] for the given structures under the same illumination that was used in the experiment.

of the measurement. Table 1 contains parameters $\beta$ and $w_{\max}$ for the two sets of data (A and B) obtained in different configurations of the s-SNOM.

From a statistical point of view, this approach centers the data values around the center of mass (first-order moments) of the data obtained from the substrate. Then, it rotates the coordinate system according to the results of the variance (second-order moments) of the data associated with the structure. This case is a two-dimensional realization of a variance calculation given by principal-component analysis [21]. The mean is

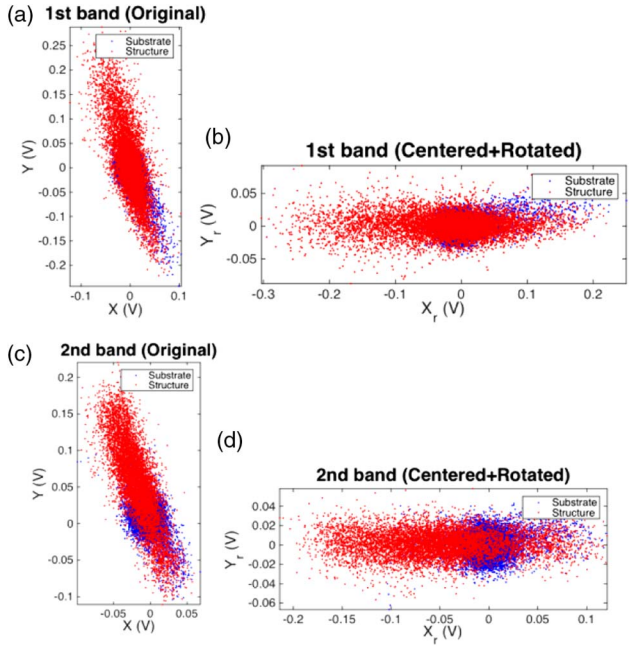


**Fig. 5.** Data cloud of the signals registered for the (a, c) first and (b, d) second sidebands for data set B. The original data are shown in plots (a) and (b). In this case, the maximum variance direction is largely misaligned with respect to the $X$ axis. Figures (c) and (d) represent the original signal rotated to align the data along the maximum-variance direction and centered to the mean of the data obtained from the substrate.

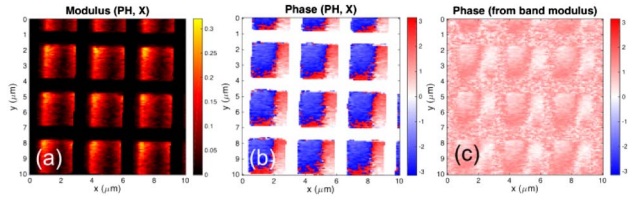


**Fig. 6.** (a) Near-field modulus and (b) phase, corresponding to the square-patches structures for data set B. Plot (c) corresponds to the results of Eq. (3) for the unsigned modulus of the signal.

subtracted from the original data, and the covariance matrix is diagonalized to obtain the orthogonal directions of the variance.

## 4. GLOBAL PHASE AND REFERENCE MIRROR POSITION

Equation (4) includes the explicit dependence of the phase of the near field, $\phi(x, y)$, on the overall phase, $\Psi_G$. This global phase is related to the mean position of the vibrating mirror at the interferometer. This mean position can be easily changed by varying the DC component driving the piezoelectric stage where the mirror is attached (see Fig. 1). In our system, the sample is moved under a static illumination, and also the position of the vibrating cantilever is fixed. Therefore, the global phase should not change over the whole scanning window. From a measurement point of view, and taking into account

Eq. (4), any change in the phase offset, $\Psi_G$, should be compensated by the phase contribution retrieved from the $\tan^{-1}$ evaluation involving the measured signals. Although the relative phase variations between different locations on the sample remain the same, the actual phase map could differ when considering different mirror positions, mainly because the location on the sample where the phase is wrapped within the usual $2\pi$ range varies with $\Psi_G$, as happens when comparing the phase maps obtained from data sets A and B [see Figs. 4(d) and 6(b)]. To analyze this fact, we have presented the results in the complex plane representing the electric field, $E_z$ [Eq. (2)], where the two sideband signals retrieved from the s-SNOM represent the real (+2 nd band) and imaginary (-1st band) parts. What we obtain is a data cloud, where each point in the cloud corresponds to a position in the sample. In this representation, the definition and location of the origin for the signal are again important. As previously, we have distinguished the substrate and metallic patch contributions, and we have used the substrate signals to center this data cloud around the mean value obtained for those signals measured at the substrate. The global phase is also responsible for the signal map distributions of the first and second bands. This is also revealed in Figs. 3(b), 3(d), and 3(f), where the data cloud shows a region oriented toward the lower left corner that corresponds with the existence of four amplitude regions in the second band map of Fig. 2.

For each point in this data cloud, its distance to the origin is proportional to the modulus of the electric field, $E_z$, and its angle with respect to the positive $X$ axis, $\Phi(x, y)$, is related to its phase, $\phi(x, y)$, through Eqs. (4) and (5). Once the data are presented, the next step is to relate the orientation of the cloud and the reference mirror location. To do that, it is possible to apply a similar method as before, obtaining the angle along the maximum or minimum variance directions for those data points belonging to the structure. However, due to the special shape of the data cloud, we applied another parameter to obtain this orientation. The proposed parameter is defined by calculating the mean value of the modulus for those data points included in an angular sector as a function of the orientation of this angular sector (see Fig. 7). Mathematically, this function can be given as

$$F(\theta) = \frac{1}{M_{[\theta,\theta+\Delta\theta)}} \sum_{j\in[\theta,\theta+\Delta\theta)} |E_{z,j}|, \tag{7}$$

where the sum is carried out within the angular sector $[\theta, \theta + \Delta\theta)$, and $M_{[\theta,\theta+\Delta\theta)}$ is the number of points within this angular sector. For the data sets considered in this paper, $F(\theta)$ presents two local minima located about 180° apart. By properly selecting the appropriate minimum, it is possible to define an angular orientation for the electric-field data cloud. Figure 7 shows the data distribution for a single position of the mirror, as well as the orientation of the cloud. We also have represented the variation of a normalized version of the orientation function, $F(\theta)$, along the full angular range. The value of $\Delta\theta$ has been set to 4°.

We have collected 12 measurements at different mirror positions from the same sample size that comprised four metallic square patches, selected from the same sample as in the previous section, in an s-SNOM configuration similar to that obtained for data set A. Since our s-SNOM system currently does not provide $X$ and $Y$ components of the signal for both sidebands, we have zeroed the phase of the lock-in amplifier before each data set as a way to speed up the acquisition and avoid stability issues. This zeroing was always made using the same location on the patch, with an uncertainty of about 250 nm caused by position drifting of the sample during the measurement. Considering the findings of our previous section, this procedure made it possible to use only the $X$ component from the lock-in amplifier for both bands. The data positions have been selected to cover a total phase shift of $2\pi$ by moving the mirror in steps of around 500 nm.

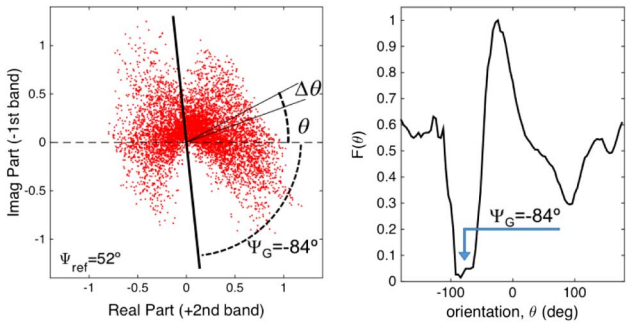


**Fig. 7.** Left: distribution of the near field for a specific position of the reference mirror. Each point defines the modulus and phase of the electric field at a given location on the sample. Right: angular representation of the normalized function $F(\theta)$ for the mirror position presented in the left plot.

The mean location of the mirror was set using the piezoelectric drive, registering the location of the mirror when the AFM scan began and ended, and considering the mean value of this range. The modulation amplitude that has been used when combining the two sidebands was also registered from the piezostage capacitance sensor signal using a digital multimeter. This provided a value of $\gamma = 1.92$. Therefore, signals from the first and second side bands need to be scaled by a factor of 1.72 and 2.99, respectively [corresponding to the values of $1/J_1(\gamma)$ and $1/J_2(\gamma)$]. All this scaling and normalization

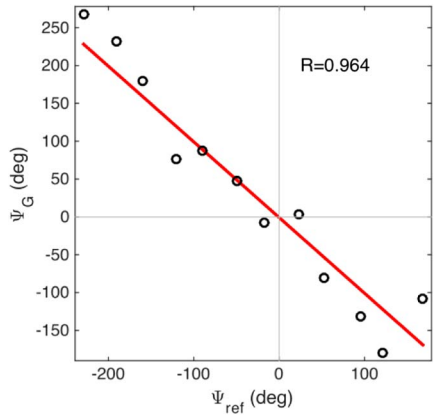


**Fig. 8.** Calculated phase, $\Psi_G$, for different positions of the reference mirror. The origin of $\Psi_G$ is arbitrary, but it can be related to the position of a predetermined interference situation when the mirror is not vibrating.

has been taken into account prior to the angular orientation evaluation.

Figure 8 shows the calculated angles for the mirror positions. A shift of 229° in $\Psi_{ref}$ has been made to make the fitted straight line pass through the origin. This fitting represents the best straight line fitted to the data, constrained to a fixed value of the slope equal to −1, as should happen when interpreting the global phase angle in Eq. (4). The correlation factor of the linear fitting is $R = 0.964$.

## 5. CONCLUSIONS

The pseudo-heterodyne detection technique in s-SNOM systems is of interest because it allows a faster data acquisition than homodyne techniques do. Then, in a single scan, it is possible to register the real and imaginary parts of the electric near field, $E_z$, on the sample.

The consideration of the signal provided by a s-SNOM system working in pseudo-heterodyne mode as having a two-dimensional character (modulus, $R$, and angle, $\alpha$; or $X$ and $Y$ components) makes it possible to obtain signed signal values. This fact expands the range of the phase accessible from pseudo-heterodyne techniques. Even in the case where the angle of the signal cannot be adjusted or zeroed, the retrieval of raster scan data for both $X$ and $Y$ components makes possible a post-processing analysis. In this analysis, the data are represented as a cloud distribution, and maximum and minimum variance directions are calculated. This calculation makes it possible to rotate the data to align them along the maximum variance direction and consider the projection along this direction as a good estimation of the signed modulus. At the same time, this approach makes it possible to quantify the quality of this projection by calculating the amount of variance included in the selected preferred direction of the maximum variance. This approach is also applicable to any other detection techniques in s-SNOM.

For the data presented in this paper, which correspond to metallic structures on a dielectric substrate, it has been possible to segment the data belonging to the metallic patches and the substrate. This differentiation makes it possible to center the data cloud at the mean value obtained for the substrate, where we are assuming a nonmeaningful near-field response. This analysis has been applied to two data sets obtained from different configurations of the s-SNOM system, which had different noise contributions. In both cases, the phase maps correspond very well to the expected results obtained from numerical simulation.

The phase retrieval is also affected by a global phase contribution that, being constant, does not affect the relative phase maps typically obtained from s-SNOM measurement. However, this global phase can affect those locations where phase maps wrap within the $2\pi$ range. By moving the central position of the reference mirror in the pseudo-heterodyne detection mode, it has been possible to register near-field maps that, after being represented in the complex plane as a data cloud, could explain the relation of the measured global phase of the data and the mirror location. The experimental results show a linear correlation factor $R = 0.964$ for the data set under analysis.

Summarizing the main results of this contribution, we demonstrated that a straightforward analysis of the data cloud obtained when combining the signal from $X$ and $Y$ components of the lock-in amplifier can provide a simple method to improve the reliability and quality of measurements in s-SNOM. Also, an analysis of the data cloud obtained when representing the complex electric field has made it possible to obtain the overall phase, depending on the particular position of the reference mirror.

**Funding.** Ministerio de Economía y Competitividad (MINECO) (PR201500063, TEC2013-40442); University of North Carolina at Charlotte.

**Acknowledgment.** This work has been done during a research stay of Javier Alda at the University of North Carolina at Charlotte (North Carolina, USA).

## REFERENCES

1. J. Atkin, S. Berweger, A. Jones, and M. Raschke, "Nano-optical imaging and spectroscopy of order, phases, and domains in complex solids," Adv. Phys. **61**, 745–842 (2012).
2. S. Stanciu, D. Tranca, L. Tarpani, G. Stanciu, R. Hristu, and L. Latterini, "Investigations on organic fluorophore doped silica nanoparticles by apertureless scanning near-field optical microscopy," in *16th International Conference on Transparent Optical Networks (ICTON)* (2014), pp. 1–4.
3. A. Singh, G. Ctistis, S. R. Huisman, J. P. Korterik, A. P. Mosk, J. L. Herek, and P. W. H. Pinkse, "Observation of nonlinear bands in near-field scanning optical microscopy of a photonic-crystal waveguide," J. Appl. Phys. **117**, 033104 (2015).
4. G. Németh, D. Datz, H. M. Tóháti, Á. Pekker, and K. Kamarás, "Scattering near-field optical microscopy on metallic and semiconducting carbon nanotube bundles in the infrared," Phys. Status Solidi B **253**, 2413–2416 (2016).
5. S. G. Stanciu, M. Costache, D. E. Tranca, R. Hristu, M. Popescu, and G. A. Stanciu, "Amplitude and phase reconstruction issues in scattering scanning near-field optical microscopy," Sci. Bull. Politeh. Univ. Bucharest Ser. A **78**, 235–244 (2016).
6. R. Olmon, P. Krenz, A. Jones, G. Boreman, and M. Raschke, "Near-field imaging of optical antenna modes in the mid-infrared," Opt. Express **16**, 20295–20305 (2008).
7. R. L. Olmon, M. Rang, P. Krenz, B. A. Lail, L. V. Saraf, G. D. Boreman, and M. B. Raschke, "Determination of the electric-field, magnetic-field, and electric-current distributions of infrared optical antennas: a near-field optical vector network analyzer," Phys. Rev. Lett. **105**, 167403 (2010).
8. A. Ravichandran, E. C. Kinzel, J. C. Ginn, J. A. D'Archangel, E. Z. Tucker, B. A. Lail, M. B. Raschke, and G. D. Boreman, "Numerical modeling of scattering type scanning near-field optical microscopy," Proc. SPIE **8815**, 88150S (2013).
9. D. Tranca, S. G. Stanciu, R. Hristu, C. Stoichita, and G. A. Stanciu, "Amplitude and phase reconstruction issues in scattering scanning near-field optical microscopy," Sci. Bull. Politeh. Univ. Bucharest Ser. A **78**, 253–262 (2016).
10. B. Deutsch, R. Hillenbrand, and L. Novotny, "Near-field amplitude and phase recovery using phase-shifting interferometry," Opt. Express **16**, 494–501 (2008).
11. P. Krenz, R. Olmon, B. Lail, M. Raschke, and G. Boreman, "Near-field measurements of infrared coplanar strip transmission line attenuation and propagation constants," Opt. Express **18**, 21678–21686 (2010).
12. N. Ocelic, A. Huber, and R. Hillenbrand, "Pseudoheterodyne detection for background-free near-field spectroscopy," Appl. Phys. Lett. **89**, 101124 (2006).

13. R. Krutokhvostov, A. Govyadinov, J. Stielgler, F. Huth, A. Chuvilin, P. Carney, and R. Hillenbrand, "Enhanced resolution in subsurface near-field optical microscopy," Opt. Express **20**, 593–600 (2012).
14. P. Alonso-González, P. Albella, F. Golmar, L. Arzubiaga, F. Casanova, L. Hueso, J. Aizpurua, and R. Hillenbrand, "Visualizing the near-field coupling and interference of bonding and antibonding modes in infrared dimer nanoantennas," Opt. Express **21**, 1270–1280 (2013).
15. M. Schnell, A. Garcia-Etxarri, A. Huber, K. Crozier, A. Borisov, J. Aizpurua, and R. Hillenbrand, "Amplitude and phase-resolved near-field mapping of infrared antenna modes by transmission-mode scattering-type near-field microscopy," J. Phys. Chem. C **114**, 7341–7345 (2010).
16. M. Schnell, P. Sarriguarte, T. Neuman, A. Khanikaev, G. Shvets, J. Aizpurua, and R. Hillenbrand, "Real–space mapping of the chiral near-field distribution in spiral antennas and planar metasurfaces," Nano Lett. **16**, 663–670 (2016).
17. L. Gomez, R. Bachelot, A. Bouhelier, G. Wiederrecht, S. Chang, S. Gray, F. Hua, S. Jeon, J. Rogers, M. Castro, S. Blaize, I. Stefanon, G. Lerondel, and P. Royer, "Apertureless scanning near-field optical microscopy: a comparison between homodyne and heterodyne approaches," J. Opt. Soc. Am. B **23**, 823–833 (2006).
18. J. M. López-Alonso, B. Monacelli, J. Alda, and G. Boreman, "Infrared laser beam temporal fluctuations: characterization and filtering," Opt. Eng. **44**, 054203 (2005).
19. D. E. Tranca, C. Stoichita, R. Hristu, S. G. Stanciu, and G. A. Stanciu, "A study on the image contrast of pseudo-heterodyned scattering scanning near-field optical microscopy," Opt. Express **22**, 1687–1696 (2014).
20. M. Esslinger, J. Dorfmuller, W. Khunsin, R. Vogelgesang, and K. Kern, "Background-free imaging of plasmonic structures with cross-polarized apertureless scanning near-field optical microscopy," Rev. Sci. Instrum. **83**, 033704 (2012).
21. J. M. López-Alonso, J. Alda, and E. Bernabéu, "Principal-component characterization of noise for infrared images," Appl. Opt. **41**, 320–331 (2002).
22. I. Horcas, R. Fernandez, J. M. Gomez-Rodriguez, J. Colchero, J. Gomez-Herrero, and A. M. Baro, "WSXM: a software for scanning probe microscopy and a tool for nanotechnology," Rev. Sci. Instrum. **78**, 013705 (2007).
23. Czech Metrology Institute, Gwyddion 2.43, http://gwyddion.net.
24. The MathWorks Inc., MATLAB, http://www.mathworks.com.
25. Ansys Inc., HFSS, http://www.ansys.com/Products/Electronics/ANSYS-HFSS.